Article

Engineering Spin Polarization of the Surface-Adsorbed Fe Atom by Intercalating a Transition Metal Atom into the MoS$_2$ Bilayer for Enhanced Nitrogen Reduction

Yuqin Zhang, Da Wang, Guanping Wei, Baolei Li, Zongchang Mao, Si-Min Xu, Shaobin Tang,* Jun Jiang,* Zhenyu Li, Xijun Wang, and Xin Xu*

Cite This: *JACS Au* 2024, 4, 1509−1520

Read Online

ACCESS | Metrics & More | Article Recommendations | Supporting Information

ABSTRACT: The precise control of spin states in transition metal (TM)-based single-atom catalysts (SACs) is crucial for advancing the functionality of electrocatalysts, yet it presents significant scientific challenges. Using density functional theory (DFT) calculations, we propose a novel mechanism to precisely modulate the spin state of the surface-adsorbed Fe atom on the MoS$_2$ bilayer. This is achieved by strategically intercalating a TM atom into the interlayer space of the MoS$_2$ bilayer. Our results show that these strategically intercalated TM atoms can induce a substantial interfacial charge polarization, thereby effectively controlling the charge transfer and spin polarization on the surface Fe site. In particular, by varying the identity of the intercalated TM atoms and their vacancy filling site, a continuous modulation of the spin states of the surface Fe site from low to medium to high can be achieved, which can be accurately described using descriptors composed of readily accessible intrinsic properties of materials. Using the electrochemical dinitrogen reduction reaction (eNRR) as a prototypical reaction, we discovered a universal volcano-like relation between the tuned spin and the catalytic activity of Fe-based SACs. This finding contrasts with the linear scaling relationships commonly seen in traditional studies and offers a robust new approach to modulating the activity of SACs through interfacial engineering.

KEYWORDS: *single-atom catalysis, charge polarization, spin modulation, atom intercalation, bilayer MoS$_2$*
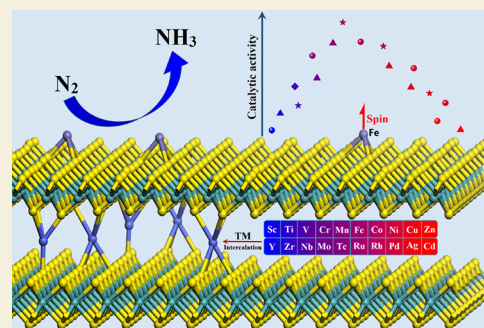
1. INTRODUCTION

Single-atom catalysts (SACs) are gaining prominence in the field of electrocatalysis, chiefly due to their exceptional atomic utilization efficiency and distinctly defined active centers.[1−6] This emerging class of catalysts, especially those involving transition metal (TM) atoms, has been recognized for its potential to revolutionize catalytic processes. One critical aspect underpinning the catalytic performance of SACs is the spin state of these active TM centers.[7−13] This spin state, intrinsically linked to the catalytic behavior, offers a vital parameter in the rational design and optimization of the catalysts. As such, the importance of effectively modulating the spin state at the TM atom site is paramount. However, this task presents significant challenges, making it a focal point of current research and development in the field.

Substantial efforts have been dedicated to the modulation of spin states at the active sites by employing a variety of techniques. These include chemical doping,[13,14] coordination environment modulation,[15,16] edge and defect engineering,[17] adsorption of neighboring metal atom,[18,19] and the application of external magnetic field.[13,20,21] However, these conventional approaches have offered only limited flexibility in tuning the spin states. A recent progress has been made to modulate the

electronic spin moments of Mo atoms exposed on the basal plane of MoS$_2$ by utilizing a single-atom promoter (SAP). This technique has shown remarkable performance in numerically tuning spin moments across a broad spectrum, demonstrating potential applications in various catalytic processes.[22] Despite all of these advances, there remains a need for an inherently more convenient and continuously modulating strategy. Such a strategy would enable a more precise design and modulation of the spin state at the active sites.

Recent advancements have seen the intercalation of atoms into layered transition metal dichalcogenides (TMDs), heralding a new class of covalently bonded materials with significant potential in energy and electronics sectors.[23−25] The incorporation of metal atoms not only enhances the electronic and magnetic properties of these materials due to an interfacial effect,[23,26] but also markedly improves their electrocatalytic
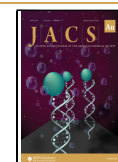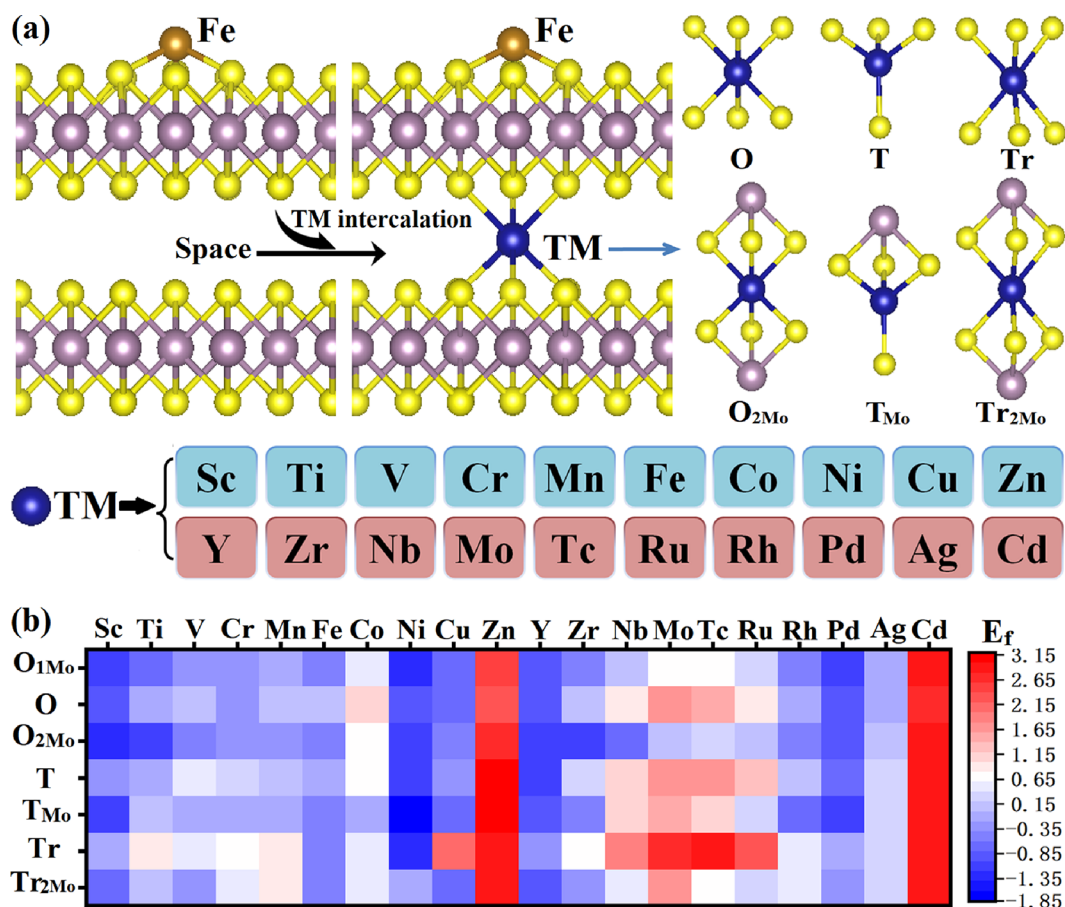
Figure 1. (a) Left: schematic illustration of adding a TM atom into the interlayer space of the MoS_2 bilayer in the Fe @ bilayer MoS_2 system. Yellow, purple, gold, and blue spheres represent S, Mo, Fe, and TM atoms, respectively. Right: illustration of the octahedral (defined as **O**), tetrahedral (**T**), and trigonal-prismatic (**Tr**) vacancy sites, and these filling sites with the TM atom pointing to the Mo (O_{2Mo}, T_{MO}, and Tr_{2Mo}, respectively). Bottom: illustration of the 3d and 4d TM atoms that are used to fill the interlayer space of the bilayer MoS_2. (b) Heatmap plot of the formation energies (E_f) of the intercalated metal atoms for all TM atoms and filling patterns.

performance.[27,28] More importantly, the metal atoms confined in bilayer TMDs possess high stability because of the chainmail-like protective structure, stabilizing the interstitial atoms even under extreme experimental environments.[29,30] Therefore, one may anticipate that intercalating TM atoms into the inherent interlayer spaces of layered two-dimensional (2D) materials, forming an intercalation single-atom structure, is poised to significantly modulate the electronic structures of the surface-adsorbed metal sites, thereby tuning the catalytic efficiency using the surface-adsorbed metal sites as the active centers.

The electrocatalytic dinitrogen reduction reaction (eNRR) to NH_3 under ambient conditions, powered by renewable energy sources, is emerging as a viable alternative to the energy- and carbon-intensive Haber–Bosch process.[31,32] However, the eNRR faces challenges due to the strong N≡N bond and slow reaction kinetics, necessitating high-performance catalysts capable of activating and efficiently converting N_2 into NH_3 under mild conditions.[33−37] Among the various TM-based SACs explored for NRR, Fe has garnered extensive attention due to its critical role in the FeMo-cofactor of nitrogenases for N_2 binding and its earth abundance.[12,38,39] More importantly, Fe sites could exhibit a diverse range of spin configurations, including low,[40,41] medium,[42] and high spin states,[12,43] leading to a substantial effect on its catalytic behavior. However, the development of

an effective strategy for precisely tuning the spin state of Fe, along with a comprehensive understanding of the corresponding modulation mechanism, remains a challenge that has yet to be fully addressed.

Herein, utilizing high-throughput DFT calculations, we first demonstrated a significant modulation of electronic spin moments of surface Fe atoms by intercalating a single TM atom into the interlayer space of the MoS_2 bilayer. Our investigation, encompassing 20 different 3d and 4d TM atoms across seven distinct intercalation patterns, revealed that a TM atom intercalated into the MoS_2 bilayers can initiate a long-range charge polarization. This polarization facilitates charge transfer from the TM atom to the Fe atom through the semiconducting sulfur–molybdenum–sulfur (S−Mo−S) layers. As a result, this charge transfer between Fe and intercalated TM atoms alters the spin-polarized d-electronic states of the Fe atom, thus enabling the tuning of its spin moments over a wide range of values. Furthermore, based on the intrinsic atomic properties, we identified an effective data-driven descriptor to accurately predict the electronic spin. Taking the eNRR as a model reaction, we constructed a universal volcano-like relation between the tunable spin moments of Fe and the corresponding catalytic activity, which distinctly differs from the linear scaling relation identified in previous studies.[9,15,44,45] Notably, we also

showcased that the Fe atom with medium spin states can largely boost the N_2-to-NH_3 conversion.

2. METHODS

2.1. Computational Method

All calculations were performed using the projector augmented wave method (PAW)[46] as implemented in the Vienna *ab initio* simulation package (VASP).[47] The generalized gradient approximation in the form of Perdew−Burke−Ernzerhof (PBE)[48] was used to describe the exchange-correction potential. A cutoff energy of 450 eV for the plane-wave basis was adopted. Spin polarization for all of the calculations was used. The DFT-D2 method by Grimme[49] was employed so that the effect of long-range van der Waals (vdW) interactions was considered. During geometry optimization, the atomic structures were fully released. The converging tolerance for forces on all atoms is less than 0.02 eV/Å, and the energy convergence criterion was set to 1×10^{-5} eV. A *z*-direction vacuum space of at least 16 Å was used for avoiding interactions between periodic images. A $3 \times 3 \times 1$ grid centered at the Γ point was used to sample the Brillouin zone for geometry relaxation. Atomic charges were analyzed based on Bader's charge population.[50,51] Atomic spin moments were obtained by using the state-of-the-art density-derived electrostatic and chemical (DDEC06) atomic population analysis method.[52,53] To evaluate the thermal stability of the intercalated TM atoms on the interlayer space of the MoS_2 bilayer, *ab initio* molecular dynamics (AIMD) simulations were performed in the canonical ensemble (NVT) with a time step of 1 fs. Two distinct temperatures, 600 and 900 K, were considered to evaluate the thermal stability under high temperature.

2.2. Structural Model

To mimic the intercalation of TM atom into the interlayer of a bilayer TMD, supercell ($4 \times 4 \times 1$) models of the 2H-MoS_2 phase were used. Test calculations showed that increasing the supercell size has a negligible effect on the spin moments of Fe (see Table S1 in the Supporting Information). In the bilayer structure of TMDs, the interlayer space typically comprises vacancies of various geometries, including octahedral, tetrahedral, or trigonal-prismatic vacancies,[54] depending on the interlayer stacking pattern between two TMD monolayer. Consequently, in our study, we focused primarily on these three types of vacancies for filling the TM atoms. For the octahedral and trigonal-prismatic vacancies, the intercalated TM atoms are coordinated with six S atoms, while for the tetrahedral one, the TM atoms have four coordinated S atoms. For each vacancy site, the occupied TM atoms contain two filling configurations: one where the TM atom points to the hexagon center of six neighboring S−Mo bonds, defined as **O**, **T**, and **Tr** patterns for octahedral, tetrahedral, and trigonal-prismatic vacancies, respectively; the other one where the TM atom points to the Mo atom in the Mo layer of MoS_2, namely **O_{2Mo}**, **T_{Mo}**, and **Tr_{2Mo}** patterns for the corresponding vacancy sites. Additionally, a third filling structure of the **O** pattern was considered, where near the Fe side, the TM atom points to the Mo atom, while for the opposite side, the TM atom points to the hexagon center (named **O_{1Mo}**). Accordingly, seven filling configurations (or patterns)—**O**, **O_{1Mo}**, **O_{2Mo}**, **T**, **T_{Mo}**, **Tr**, and **Tr_{2Mo}**—were constructed for each intercalated TM atom. The surface-adsorbed single Fe atom, placed on top of the Mo atom and connected with three neighboring S atoms, was primarily constructed to simulate the SAC. Figure 1a presents the schematic illustration for intercalating a TM atom into the interlayer space of the MoS_2 bilayer with a surface Fe atom and the corresponding six vacancy filling configurations.

To elucidate the impact of intercalated metal atoms on the electronic structures at the Fe sites, we explored a comprehensive set of 3d and 4d transition metal atoms, including the TM elements of period 4 (Sc, Ti, V, Cr, Mn, Fe, Co, Ni, Cu, and Zn) and period 5 (Y, Zr, Nb, Mo, Tc, Ru, Rh, Pd, Ad, and Cd). Combining the 20 TM atoms and seven types of occupied vacancy sites (**O**, **O_{2Mo}**, **O_{1Mo}**, **T**, **T_{Mo}**, **Tr**, and **Tr_{2Mo}**), there are 140 sampling data points (see Figures S1−S8 for detail of structures). The details of the calculations on the

free energy and catalytic activity for eNRR are elaborated in the Supporting Information.

To further verify the generalizability of the tuned electronic structures of Fe, we performed additional Heyd−Scuseria−Ernzerhof screened hybrid density functional (HSE06[55,56]) and GGA+U (with U of 4 eV and on-site exchange constant J of 1 eV[57,58]) calculations on selected systems (see details in Table S2−S4 and Figure S9−S11). The Poisson−Boltmann implicit solvation model[59] as implemented in VASPsol was used, when considering a solvent environment, with the dielectric constant ε of water as 80.

Following previous models,[23] when the effect of concentration of intercalated TM atom (σ) is considered, the $2a \times \sqrt{3}\,a$ periodic lattice of 2H-MoS_2 was used to simulate $\sigma = 25\%$, 50%, and 75%, whereas for $\sigma = 33.3\%$ and 66.7%, the $\sqrt{3} \times \sqrt{3}\,a$ superlattice of MoS_2 was adopted. The parameter σ is defined as the percentage of the initial total vacancy sites occupied by the intercalated TM atoms.

2.3. SISSO Model

To accurately predict the electronic spin moments of Fe and establish a quantitative structure−property relationship based on a small data set, we applied an interpretable machine learning method, namely, the compressed sensing and symbolic regression, sure independence screening and sparsifying operator (SISSO),[60] to suggest effective descriptors and unveil the mathematical correlations between input features and target properties (see the Supporting Information for more details).

3. RESULTS AND DISCUSSION

3.1. Stability of TM Atoms Intercalated into the MoS_2 Bilayer

Our calculations for the relative total energies of MoS_2 structures with intercalated TM atoms across different configurations—**O_{2Mo}**, **O_{1Mo}**, **T**, **T_{Mo}**, **Tr**, and **Tr_{2Mo}**—in comparison to the structure with **O** pattern (see Figure S12), reveal a notable trend. Generally, for all considered 3d and 4d TM atoms, excluding Co, Ni, Cu, and Rh, configurations with the octahedral vacancy site demonstrate more stability than those with the tetrahedral and trigonal-prismatic structures. Furthermore, compared to the pure **O** site, a majority of the TM atoms exhibit a preference for the **O_{2Mo}** or **O_{1Mo}** sites, where the TM atom points to the Mo atom. Among the 7 evaluated filling patterns, the trigonal-prismatic configuration exhibits the lowest stability.

To evaluate the thermodynamic stability of the intercalated metal atoms, we calculated the formation energy of TM atoms sandwiched between the MoS_2 bilayer by $E_f = E(TM\text{-}2MoS_2) - 2E(MoS_2) - E(TM)$, where $E(TM\text{-}2MoS_2)$, $E(MoS_2)$, and $E(TM)$ are the total energies of the MoS_2 bilayer with the filled TM atom, pristine MoS_2 monolayer, and metal atom in its most stable bulk structure, respectively. According to this definition, a negative formation energy ($E_f < 0$) indicates that the intercalated TM atom is thermodynamically more stable than in its bulk phase. Our calculations, as illustrated in Figure 1b, show that most TM atoms considered (excluding Zn, Mo, Tc, and Cd) can be atomically dispersed within the interlayer space of the MoS_2 bilayer, where the metal atom can adopt at least one filling pattern that is favorable, as indicated by the negative E_f value. These single TM atoms, specifically Sc, Ti, Fe, Ni, Cu, Y, Zr, Nb, Rh, and Pd, demonstrate notably high stability with E_f values lower than −0.6 eV in their most favorable filling configurations. In addition, AIMD simulations have confirmed that TM atoms with 6-fold S coordination are securely situated in the octahedral vacancy site of the MoS_2 bilayer. Notably, the geometrical structure of Fe SACs remains unchanged at 900 K even after 2 ps, as shown in Figure S13.
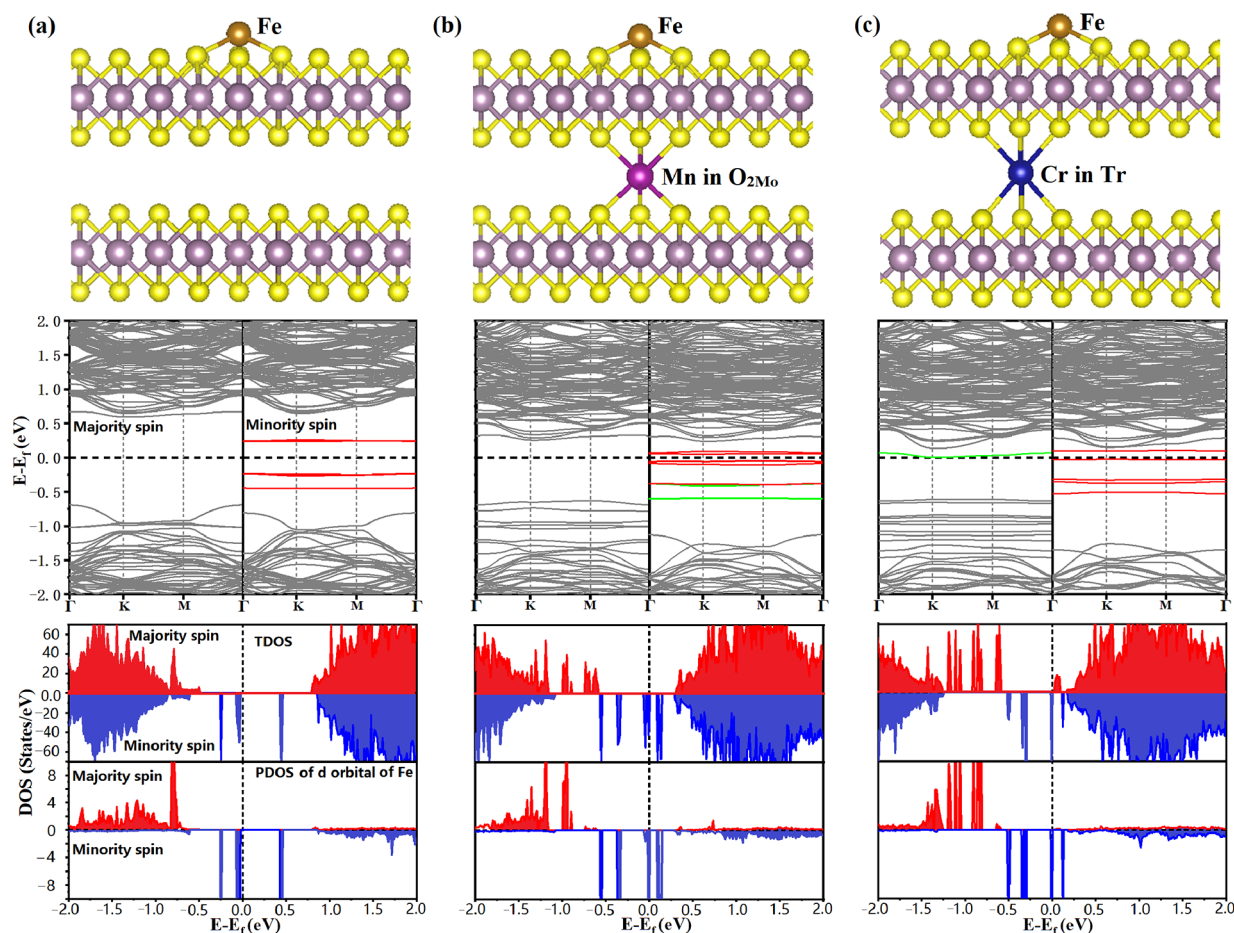
Figure 2. Geometry structures (top panel), spin-polarized band structures (middle panel), and total density of states (TDOS) and partial DOS of d orbitals of the Fe atom (bottom panel) for Fe SACs supported by the MoS$_2$ bilayer (a) without and with (b) Mn and (c) Cr intercalation. In the middle panel, the bands with red for minority spin represent the d orbitals of Fe, while in panels (b) and (c), the bands with green originate from the intercalated metal atom. The Fermi level is normalized to 0 (dashed lines) across all band structures.

Previously, many experimental methods, such as a metal-rich chemical potential,[23] modified atmospheric preesure achemcial vapor deposition (APCVD),[25] and solvent-baded intercaltion,[24] have been proposed to intercalate the metal atom into bilayer transition metal dichalcogenides. Therefore, it is anticipated that the realization of the designed metal atom intercalations into the MoS$_2$ bilayer is viable experimentally.

3.2. Effect of Single Intercalated TM Atom on the Spin State of Surface Fe Atom

We now explore the impact of intercalated TM atom on the electronic structure of the surface Fe atom adsorbed on the bilayer MoS$_2$. Figure 2a−c presents the band structures of Fe-adsorbed bilayer MoS$_2$, without and with Mn or Cr intercalation, along with the corresponding total density of state (DOS) of the material and the partial DOS (PDOS) of the d orbitals of Fe (see Figures S14−S21 for other TM atom and the intercalation pattern combinations). Clearly, the intercalated TM atoms narrow the band gap of pristine Fe SACs, which is attributed to the shift of the energy levels of the highest occupied and the lowest unoccupied d molecular orbitals (HOMO and LUMO) of Fe toward the Fermi level. Additionally, new flat states originating from the TM atom are introduced into the gap, as evidenced in the middle panel of Figure 2c and Figure S14, and in the total DOS (bottom panel of Figure 2). This reduction in the band gap could enhance the

conductivity of the material, thereby facilitating charge transfer between the MoS$_2$ bilayer substrate and the Fe active site. More importantly, the calculated PDOS shows that the d-electronic states of Fe around the Fermi level, particularly in the minority spin channel, are significantly influenced by the intercalated TM atoms. In contrast, the majority spin channel shows a smaller effect (see the bottom panel in Figure 2 and Figures S16−S21). As a result, intercalation leads to a modulation in the spin polarization behavior of the Fe atom, thus tuning its electronic spin moments.

To further elucidate the intercalation impact on the electronic structure of the Fe atom, we conducted an in-depth analysis of the charge density difference in Fe SACs on the MoS$_2$ bilayer, along with the corresponding the spin densities (see left and right panel in Figure 3a and Figures S22−S23, respectively). The charge distribution was determined by subtracting the total charge densities of Fe, the intercalated TM atom, and the remaining MoS$_2$ from the overall charge densities of the whole intercalated system. This analysis reveals the principal effects of modulation with intercalation. First, the charges of the intercalated TM atoms become polarized due to the interaction with the MoS$_2$ bilayer. This charge polarization, in turn, initiates electron transfer from the intercalated TM to the surface Fe atom through the S−Mo−S layered structures. As a result of these processes, there is a modulation of both the charges and the electronic
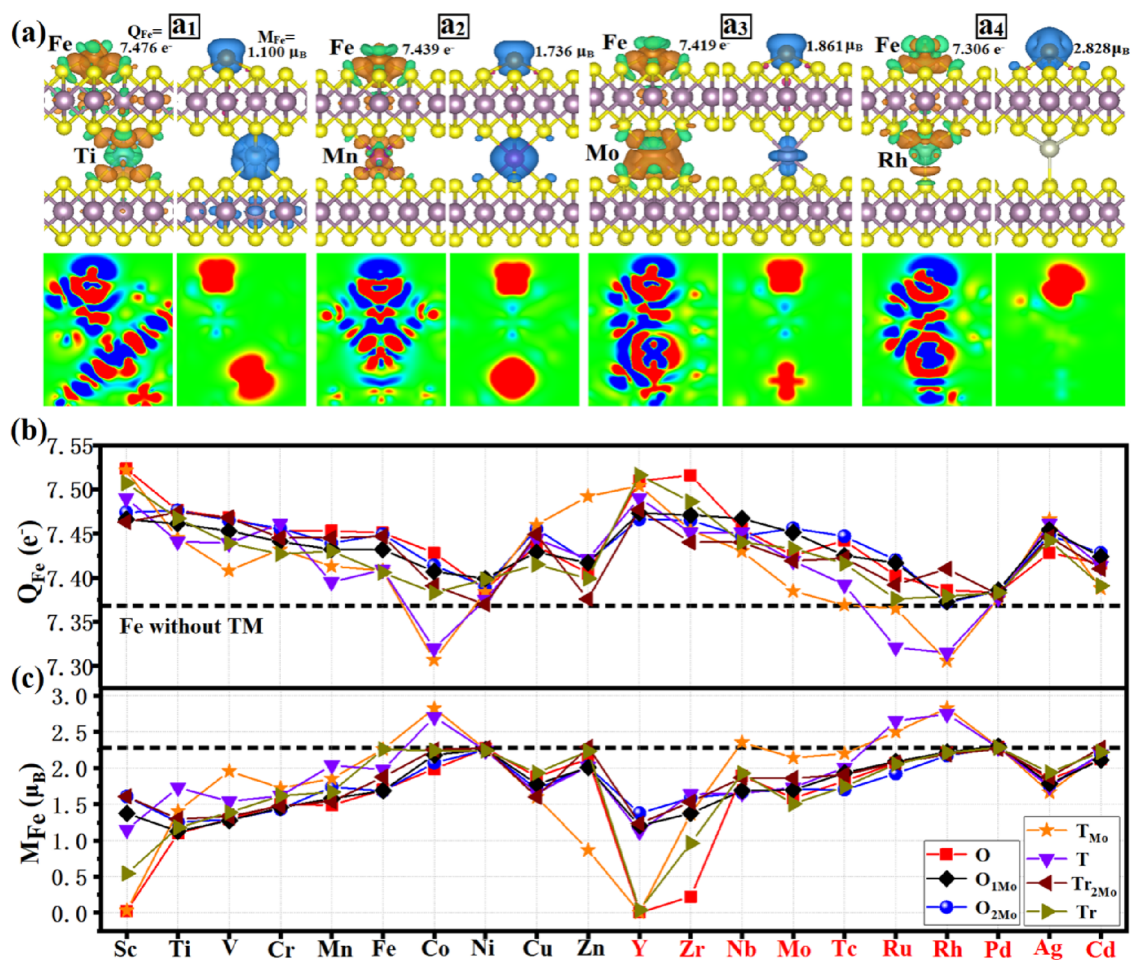
Figure 3. (a) Polarized charge distribution (left panel) and spin densities (right panel) for the surface-adsorbed Fe atom on the MoS_2 bilayer with Ti (a1), Mn (a2), Mo (a3), and Rh (a4) intercalation. In the left panels of (a1)−(a4), the orange and green foams represent electron accumulation and depletion, respectively, while in the right panel, the blue foams define the majority spin. The Bader charge (Q_{Fe}) and spin moment (M_{Fe}) values of Fe are provided. In the bottom panels of panels (a1)−(a4), the slices of charge and spin distribution along the plane across Fe, TM, and their neighboring Mo atoms are presented. All isosurface values are set to 0.005 $e/Å^3$. Changes in (b) Q_{Fe} and (c) M_{Fe} of Fe as a function of the intercalated TM atoms for seven vacancy filling patterns. The horizontal dashed line marks the baseline values of Fe without TM intercalation.

spin moments of the Fe atom. These findings are crucial, as they provide insights into the dynamic interactions and electronic structural changes occurring on the surface Fe site.

To quantitatively analyze the modulation effect with intercalation, we computed the Bader charge (Q_{Fe}) and spin moment (M_{Fe}) values of the surface Fe atom. This analysis encompassed 20 TM atoms across 7 distinct filling configurations as introduced above, totaling 140 data points, as illustrated in Figure 3b. Our comparative assessment of the 7 filling configurations revealed a consistent trend in the changes of Q_{Fe} and M_{Fe}, versus the intercalated TM atoms. Notably, we observed a decrease in Q_{Fe} when transitioning from Sc to Ni for the 3d metals (and from Y to Pd in the case of the 4d metals). This was followed by an increase when TM is changed to Cu (Ag) and then another decrease when the TM atom was changed to Zn (Cd). The range of these variations spanned from 7.30 to $7.52e^-$ (see the top panel in Figure 3b).

M_{Fe} (bottom panel in Figure 3c) exhibits an inverse trend compared to that of Q_{Fe}. By altering the type of intercalated TM atom and its specific intercalation pattern, M_{Fe} experiences a broad range of modulation, with values extending from approximately 0 to $2.8\mu_B$. Interestingly, in cases where TM =

Sc, Y, and Zr with an O filling pattern, the spin states of Fe are almost negligible. Therefore, the transformation of Fe spin states from low to medium and then to high spin states is precisely realized by combining the choice of TM atom and the appropriate filling configuration. When one MoS_2 layer was replaced with graphene due to its high conductivity, a wide-range tuning in spin moments was also realized (see Figure S24 for details).

3.3. Mechanisms for Modulation in Spin Moments of Fe

To reveal the origin of spin moment modulation on the Fe atom, we further delved into the charge transfer dynamics involving the intercalated TM atom, adsorbed Fe atom, and their connecting moieties. Figure 4a presents the relationship between the surplus charges of the connecting S atom (ΔQ_S), the polarized charge of the intercalated TM atom (ΔQ_{TM}), and the surplus charge of the adsorbed Fe atom (ΔQ_{Fe}) in the **O** pattern, relative to the catalyst without Fe (see Figure S25 for other filling pattern). A clear correlation among these parameters suggests the establishment of an effective charge transfer channel from the intercalated TM atom to the surface Fe site. Initially, the inverse scaling relation between ΔQ_S and ΔQ_{TM}, as depicted by the black line in Figure 4a, indicates that TM atoms donate electrons to the connecting S atoms due to
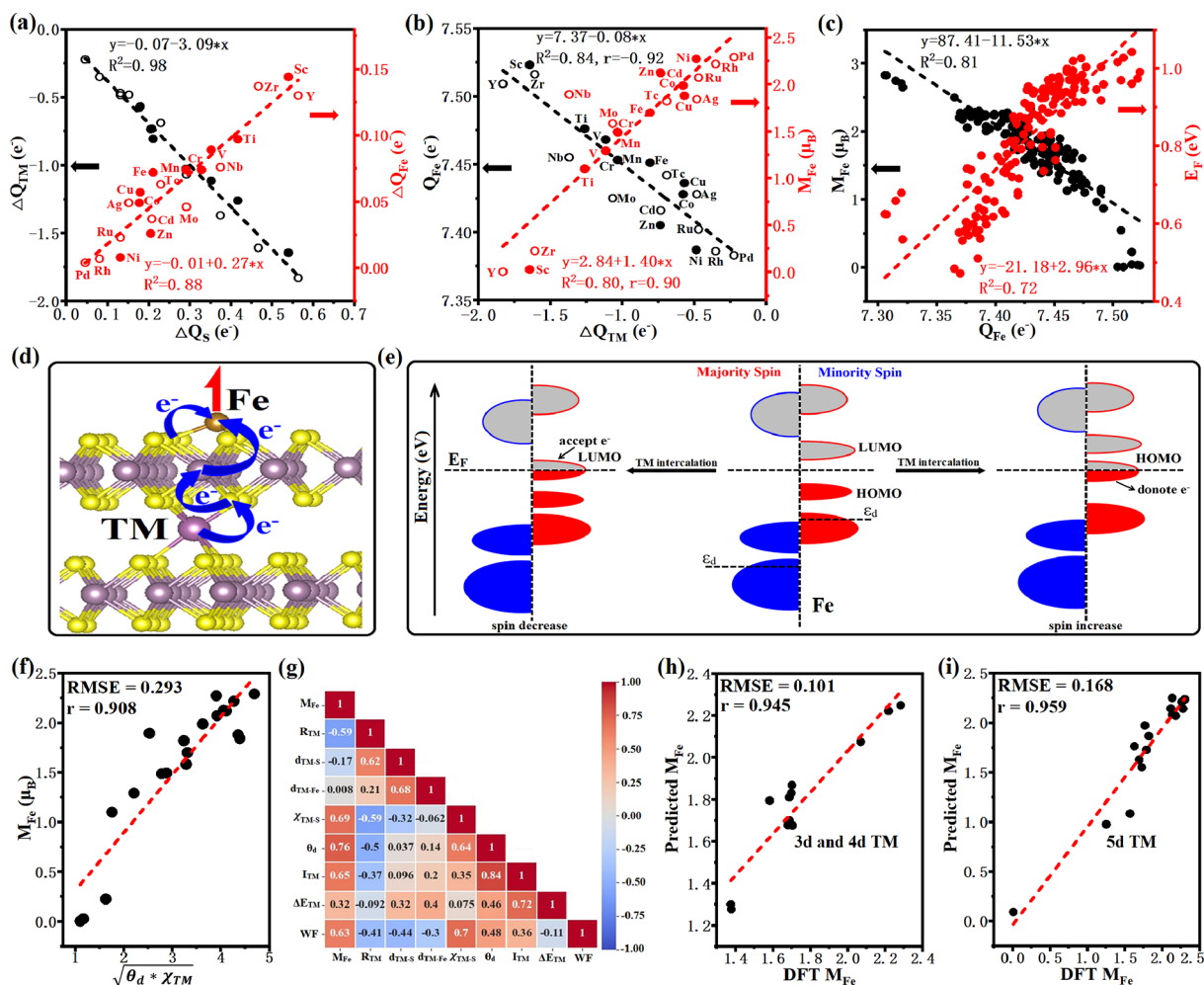
Figure 4. Scaling relations among the electronic structures of Fe, intercalated TM atoms, and the connected S atoms: (a) surplus charge of the neighboring S atom (ΔQ_S), polarized charge of the intercalated TM atom (ΔQ_{TM}), and surplus charge of the Fe atom (ΔQ_{Fe}), (b) ΔQ_{TM}, Q_{Fe}, and M_{Fe} of Fe for O filling pattern, and (c) Q_{Fe} and M_{Fe}, and the work function (WF) of substrates of Fe SACs for all considered structures. (d, e) Schematic mechanism for spin state modulation of Fe by tuning the spin-polarized d electronic states by charge communication between TM and Fe atoms. (f) Fitting performance of the descriptor $\varphi = \sqrt{\theta_d * \chi_{TM}}$, for the O filling pattern. (g) Pearson correlation coefficient matrix maps between each other of 8 primary features and these features with M_{Fe}. Comparison of DFT-computed and best SISSO model-predicted M_{Fe} on (h) the source test set and (i) the new test set with 5d TM atoms.

the intercalation interaction. Subsequently, these electrons, donated by the TM atoms to the S atoms, are further transferred to the Fe atom through the neighboring Mo and S atoms. This process is evidenced by a strong positive correlation between ΔQ_S and ΔQ_{Fe}, as shown by the red lines in Figure 4a.

It appears that the degree of charge polarization of TM atoms plays a crucial role in determining the d electronic charges of the Fe atom and thus influencing the magnitude of electronic spin moments at the Fe site. In general, a stronger charge polarization of TM atoms (corresponding to a larger net ΔQ_{TM}) leads to a higher occupation of d electrons in Fe, as illustrated by the black line in Figure 4b. This, in turn, results in smaller spin moments (depicted by the red line in Figure 4b, see Figure S26 for other patterns), a relationship further validated by an inverse scaling between M_{Fe} and Q_{Fe} (black line in Figure 4c). The change in Q_{Fe} is ascribed to the tuned Fermi level of SACs (red line in Figure 4c). Consequently, we can infer that M_{Fe} tends to decrease as the TM atom shifts from the right to the left in the periodic table due to an

increase in net ΔQ_{TM}. This trend indicates a mechanism for precisely tuning the spin state of the surface Fe atom through modulation of the charge polarization of the intercalated TM atom.

Now, we present a comprehensive physical explanation of the mechanism governing the modulation of spin states at the Fe atom, as depicted in Figure 4d. This mechanism begins with the polarization of charges in the intercalated TM atoms, which is driven by intercalation interactions with the interlayer of the MoS$_2$ bilayer. This polarization facilitates the penetration of electrons (or charges) from the TM atoms to the surface Fe atoms through the connecting S atoms and the neighboring Mo atoms. Finally, the variation of d electronic charges of Fe leads to the effective modulation of spin moments of Fe.

To gain a deeper insight into the relationship between charge and spin of Fe atoms, we compared their d electronic state-related properties across both majority and minority spin channels based on the calculated d-band center (Figure S27) and PDOS of Fe (Figures S15−S21). As depicted in a
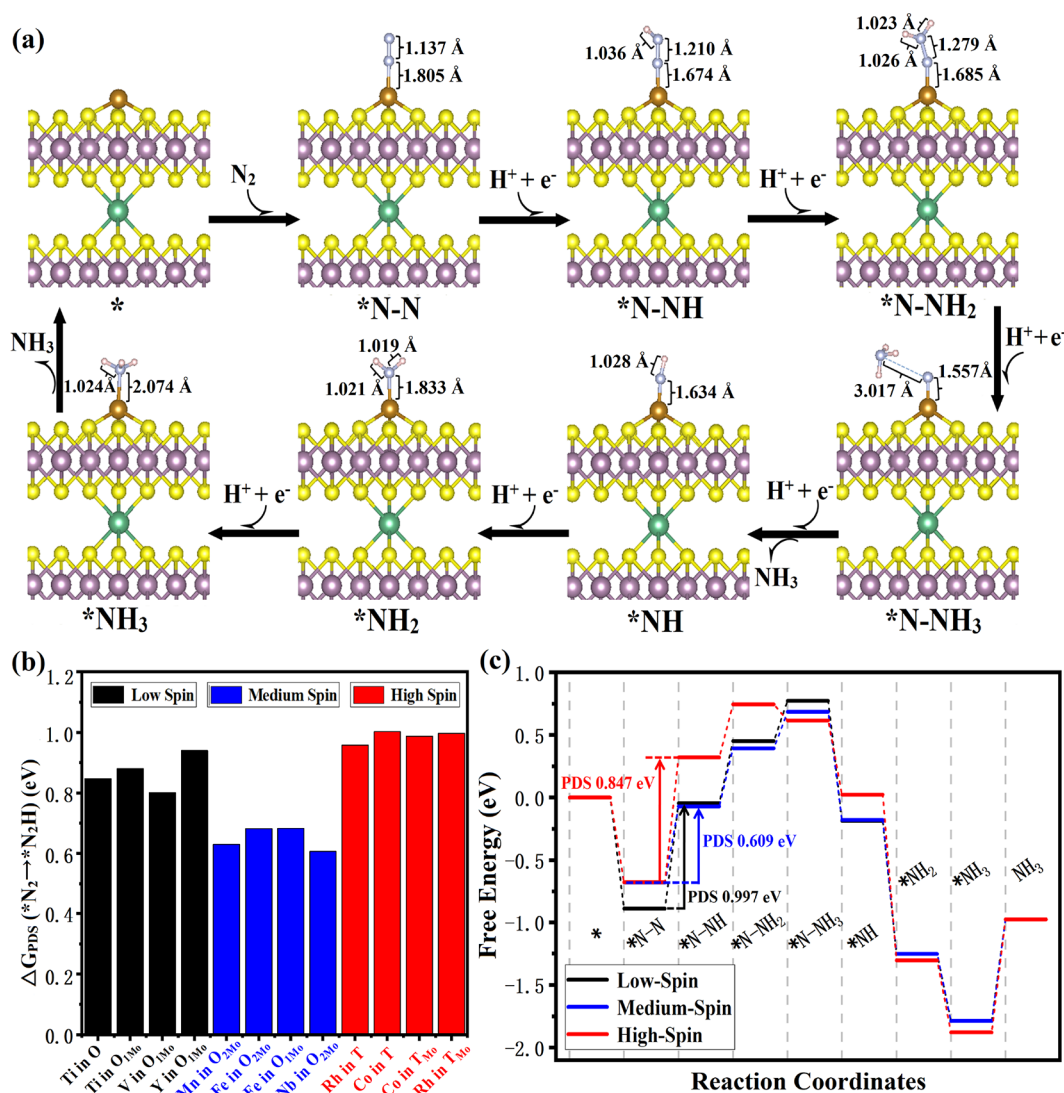
Figure 5. (a) Schematic diagram for the distal pathway of N_2 electrochemical reduction to NH_3 catalyzed by Fe SACs on TM-intercalated bilayer MoS_2 and the corresponding bond length for TM = Nb. (b) Comparison of $\Delta G_{PDS}(*N_2 \rightarrow *N_2H)$ and (c) free energy diagrams of eNRR through the distal pathway for the selected Fe SACs with low, medium, and high spin moments produced by various TM atom intercalations. In panel (c), the selected TM atoms are Ti (black line), Nb (blue), and Rh (red) in the form of O, O_{2Mo}, and T_{Mo} filling patterns, respectively. The vertical arrows denote the free energy barrier of the potential-determining step (PDS).

schematic diagram in Figure 4e, we observed two distinct differences in the d orbitals of Fe between these two spin channels (excluding the cases with near zero spin): (1) for most of TM atoms, the d-band center of the minority spin is positioned closer to the Fermi level compared to that of the majority spin; (2) the HOMO and LUMO for d orbitals of the minority spin are located near the Fermi level, whereas those for the majority spin are further away from the Fermi level. These differences indicate that the minority spin HOMO and LUMO of Fe predominantly govern its charge transfer behavior, thereby influencing the tuning of spin as TM atoms are intercalated. A more detailed discussion can be found in the Supporting Information (see also Figure S28).

3.4. Prediction of Spin Moments of the Surface-Adsorbed Fe Atom

Although a notable correlation exists between ΔQ_{TM} and M_{Fe}, as evidenced by a relatively high Pearson coefficient of $r = 0.9$ (see red line in Figure 4b), the ability to accurately predict M_{Fe} using intrinsic material properties that are readily available

without the need for complex calculations is more practical in real-world applications. This is particularly important given the challenges associated with experimental measurement of atomic charge. Inspired by previous studies,[61−63] we identified two intrinsic atomic properties of the TM atom as key determinants of charge transfer, i.e., the number of d electrons (θ_d) and electronegativity of the TM atom (χ_{TM}). We proposed a descriptor, $\varphi = \sqrt{\theta_d^* \chi_{TM}}$, to predict M_{Fe} for the O filling structures. The high Pearson correlation coefficient of $r = 0.91$ and a small root-mean-square error (RMSE) of 0.29 μ_B (Figure 4f) indicate that this descriptor, relying solely on materials' intrinsic properties, could approximately describe the spin state of Fe (see Figure S29 for other filling pattern). This allows for a quick and precise modulation of M_{Fe} by rationally adjusting the type of the intercalated TM atom rationally.

To further improve the prediction accuracy for M_{Fe} when considering all O filling structures, as shown in Figure S29c, we expanded our model beyond the initial parameters of θ_d and χ_{TM}. We incorporated 6 additional input features, encompass-

ing various intrinsic properties, geometry parameters, and binding energy of the TM atom as well as work function (W_F) of the bilayer substrate (see Table S5). Pearson correlation coefficient matrix maps show that in addition to θ_d and χ_{TM}, the ionization energy (I), and WF have a strong correlation with M_{Fe}, and these four parameters are also correlated to each other. We thus employ the 8 parameters as input features, utilizing SISSO, to suggest improved descriptors for M_{Fe} (see Tables S6 and S7 for training set and testing set, respectively).

Figure 4h showcases the superior predictive power of the top 10 3D descriptors (3 terms in the mathematical expression) for M_{Fe} as suggested by SISSO (see Table S8 for details of all models). The agreement between the predicted values and those computed via DFT are excellent. The Pearson correlation coefficients stands at 0.94, with a low RMSE of $0.1\mu_B$ (see Table S9 for prediction detail), which falls within the error range of DFT calculations. Notably, even we deliberately discard the descriptors with the term of binding energy; due to its challenging experimental measurement, the predictive accuracy of the best descriptor still remains high ($r = 0.91$, RMSE = $0.14\mu_B$) (see Table S10). These findings highlight the exciting potential of accurately predicting M_{Fe} from materials' intrinsic properties.

More intriguingly, we attempted to adapt the obtained descriptors to predict M_{Fe} on a new testing set comprising 5d TM atoms, Ta, W, Re, Os, Ir, Pt, Au, and Hg, previously not included in our training data set. Impressively, the models demonstrated robust predictive capabilities when applied to these new TM atoms, as illustrated in Figure 4i and detailed in Table S11. This remarkable performance underscores the transferability of our descriptors, highlighting their potential in broader applications beyond the initial training scope.

3.5. Dependence of the Fe Spin Moments on the Concentration of the Intercalated TM Atom

Previous studies[23] have demonstrated that covalently bonded bilayer transition metal dichalcogenides, specifically TaS_2 with self-intercalated tantalum (Ta), exhibit electronic properties that vary with the concentration of the intercalant. To this end, we further investigated the effect of the concentration of the intercalated TM atoms (σ) on M_{Fe}. In this analysis, we only focus on TM atoms from the 3d metal series occupying octahedral vacancy sites, specifically 25%, 33.3%, 50%, 66.7%, and 75% because of the stable phase as previously reported on TaS_2 experimentally (see Figures S30 and S31 for geometric structures).[23] The results reveal (see Table S12) that for many of the TM atoms considered the concentration of the intercalated TM markedly impacts the value of M_{Fe} (see Figure S32a,b for detailed discussion on the Zn atom). For each TM concentration evaluated, M_{Fe} consistently appears to be inversely proportional to the polarized charges of the TM atoms (see Figure S32c), a trend agrees well with the case of single TM atom interactions (red line in Figure 4b).

3.6. Constructing the Spin−Catalytic Activity Relationship of Fe SAC for eNRR

Taking the eNRR as a representative catalytic reaction, we examined how the intercalated TM atoms influence the catalytic activity of the Fe SACs. To this end, we computed the entire reaction pathway for N_2 reduction to NH_3 on selected Fe SACs. We specifically included three types of spin states of Fe, low, medium, and high, when choosing the systems for analysis, with three reaction mechanisms, namely, distal, alternating, and enzymatic, being considered. The distal and alternating mechanisms originate from the end-on N_2 adsorption configuration, whereas the side-on N_2 adsorption results in the enzymatic pathway (see Figure S33 for details of the mechanism). The end-on configuration for N_2 adsorption is still more stable than the side-on structure (Figure S34). Compared with the Fe SACs, most of the intercalated TM atoms could strengthen the N_2 adsorption. Figure 5a presents the geometries of the intermediates through the distal pathway of eNRR (see Figure S35 for other pathways).

Tables S13−S15 list the free energy change for all elementary steps in N_2 reduction to NH_3 through the distal, alternating, and enzymatic pathways (see Table S16 for free energy corrections). It is found that the potential-determining step (PDS) consistently involves the first protonation process from $*N_2$ to $*N_2H$. The N_2 reduction to NH_3 on the selected Fe SACs predominantly occurs through the distal or alternating pathway, as opposed to the enzymatic mechanism.

A comparison of the free energy change at the PDS ($\Delta G_{PDS}(*N_2 \rightarrow *N_2H)$) among these Fe SACs with varying spin states (illustrated in Figure 5b) reveals that a medium spin state is more conducive to the protonation of $*N_2$ to form $*N_2H$, as indicated by a lower ΔG_{PDS} compared to Fe atoms in other spin configurations. For instance, Figure 5c shows that the medium spin state of Fe, at $1.6\mu_B$, lowers the ΔG_{PDS} to 0.61 eV, being much lower than the ΔG_{PDS} values of 1.0 and 0.85 eV for the low ($1.1\mu_B$) and high spin states ($2.6\mu_B$). Additionally, compared with the high spin configuration, the desorption of NH_3 occurs more easily on Fe SACs with low and medium spin states. Interestingly, although solvation effects increase the spin moments of Fe atoms for the low and medium spin states, the main conclusion that the eNRR catalytic activity is improved by the medium spin remains unchanged (see detailed discussions in Figure S36).

To establish the correlation between M_{Fe} and the catalytic activity, we plotted the relationship between ΔG_{PDS} and spin moments of Fe for all systems considered as shown in Figure 6a (see Figure S37 for details of $\Delta G_{PDS}(*N_2 \rightarrow *N_2H)$). Interestingly, our findings diverge from previous studies[9,15,44,45,64] which suggested a linear relationship between the catalytic activity of SACs and the spin of the metal site. Instead, we obtained a volcano-like curve between ΔG_{PDS} and M_{Fe}. This suggests the existence of an optimal M_{Fe} value to achieve the lowest possible barrier for the PDS of eNRR. The volcano-shaped relation can be understood by the N_2 activation step, which controls the whole reaction process of eNRR on our Fe SACs. In general, the amount of d electrons on the active metal plays the key role in N_2 activation due to the electron "acceptance-donation" mechanism between them.[5] From the constructed volcano-like relation between Q_{Fe} and ΔG_{PDS}, a moderate d electron density of Fe is optimal for promoting the $*N_2$ activation (see Figure S38). Combining the well linear correlation of M_{Fe} with Q_{Fe} (Figure 4c), a medium spin of Fe should be beneficial to reducing the limiting-potential of eNRR. We also noted that the catalytic activity of SACs is also heavily influenced by other factors beside the spin, such as d-band center of Fe and work function of materials, leading to complicated correlation beyond that with single electronic structure-based descriptor (see detailed discussions alongside Table S17 and Figure S39).

In particular, Fe SACs with intercalated TM atoms, such as Mn, Nb, and Mo—positioned near the apex of the volcano curve—exhibit promising eNRR activity. These catalysts demonstrate the lowest limiting potential of −0.58 V among
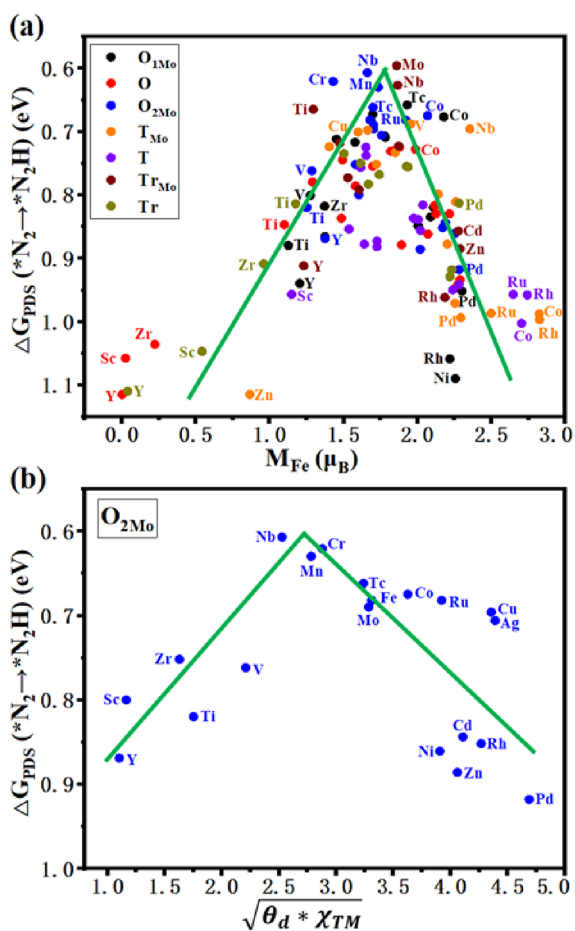
Figure 6. Volcano-shaped relationship between the free energy change of the hydrogenation step from *N$_2$ to *N$_2$H (ΔG_{PDS}(*N$_2 \rightarrow$ *N$_2$H)) and (a) M$_{Fe}$ for all TM atoms considered with different filling patterns and (b) $\varphi = \sqrt{\theta_d^* \chi_{TM}}$ for the **O$_{2Mo}$** filling pattern.

all considered catalysts. This predicted limiting potential is even lower than those observed for FeN$_3$[30] (-1.03 V) and FeN$_4$[65] (-1.3 V) embedded in graphene, single Fe atom on MoS$_2$ (-0.9 V),[66,67] and stepped Ru (0001)[65] (-0.98 V), which are considered benchmarks in metal-based catalysis, thereby highlighting the outstanding catalytic activities of the present findings.

Many previous theoretical works have constructed excellent descriptors to correlate with the electrocatalytic activity of single-atom sites based on certain intrinsic properties of materials, such as the coordination number, the electronegativity of metal atom and its coordination atom.[62,68] Herein, we proposed a descriptor, $\varphi = \sqrt{\theta_d^* \chi_{TM}}$, to predict the ΔG_{PDS} of eNRR on Fe SACs, where the θ_d and χ_{TM} are the d electrons number and electronegativity of the intercalated metal atoms, respectively. As illustrated in Figure 6b, a volcano-like relation between ΔG_{PDS} and ϕ is obtained for the O$_{2Mo}$ filling pattern (see Figure S40 for other patterns). Based on the relation, the most promising Fe SACs for eNRR are realized when the ϕ is located at about 2.75. Interestingly, an approximate volcano-shaped relation between ΔG_{PDS} and M$_{Fe}$, and ϕ is still obtained, if the ratio of Fe to intercalated TM atoms is set to 1:2 in the structural models (see Figure S41), indicating the usefulness of the present descriptor and the

importance of maintaining a moderate spin moment of the Fe atom for higher eNRR activity.

To further clarify whether the spin of the metal site predominantly influences the catalytic activity, particularly in relation to its correlation with charges, we conducted test calculations using Ni and Co as alternative active sites to Fe. In these calculations, only 3d TM atoms were used as intercalants in the **O** filling pattern within the interlayer space of the MoS$_2$ bilayer. The results show that the Ni site did not exhibit any spin moments, both before and after metal intercalations, across all of the TM atoms (Table S18). This consistently leads to a high free barrier for the *N$_2$ to *NNH step, with ΔG_{PDS} averaging 1.82 eV (Table S18). In contrast, for the Co active site, significant spin moments were observed solely with intercalated Ni atoms. The intercalation of other TM atoms led to degeneration of the spin on Co (Table S19). As expected, the induced spin moments can significantly lower the ΔG_{PDS} to 1.0 eV from approximately 1.29$-$1.61 eV in cases where the Co sites hold no spin (Table S19). Therefore, the improved catalytic activity of Fe SACs could be attributed to the finely tuned spin state at the Fe site.

Recently, two interesting theoretical works by Li et al.[69,70] reported that during the processes of the O$_2$ activation/CO oxidation on the two-dimensional materials with magnetic single Mn atoms, the spin-conservation rule was well manipulated by the synergetic charge transfer and spin selection at neighboring magnetic single-atom sites. Herein, we examined the evolution of charge and spin of Fe site-related segments during *N$_2$ and *N$_2$H adsorption as illustrated in Figures S42 and S43. The calculated results showed that the spin moments of Fe sites were mainly transferred to the MoS$_2$ substrate and/or the intercalated metal atom. The intermediates accumulated most of the electrons, which were mainly transferred from the MoS$_2$ fragments through the channel of the Fe atom. Therefore, the synergetic charge transfer, provided by the MoS$_2$ substrate, and spin selection, preserved by transferring spin from the metal center to MoS$_2$, were responsible for the observed spin-conservation.

4. CONCLUSIONS

We have achieved, for the first time, a precise modulation of the spin state of the surface-adsorbed Fe atom through interfacial charge polarization induced by the TM atom intercalated into the bilayer space of the MoS$_2$ bilayer. The intercalated TM atoms, notable for their remarkable stability, initiate a substantial charge transfer to the surface Fe atoms via the S$-$Mo$-$S layers. This process effectively modulates the spin-polarized d electronic states of Fe, thereby tuning its spin moments. Furthermore, our research has meticulously explored the impact of varying the type of intercalated TM, the pattern of filling vacancies, and the concentration of TM atoms. This comprehensive approach has enabled us to achieve a diverse range of spin moments on Fe atoms, spanning from low to medium, and ultimately to high spin states. We have also developed an innovative and efficient data-driven descriptor that utilizes easily accessible intrinsic features of TM atoms, to accurately predict the spin moments at the surface Fe sites.

Focusing on the eNRR as a model catalytic reaction, our findings unveil a previously unseen volcano-like relationship between the tuned spin moments and the catalytic activity. Here, medium spin moments of Fe are shown to significantly lower the barrier of the potential-determining step, facilitating

the hydrogenation of *N$_2$ to *NNH. This breakthrough not only establishes a robust and novel method for the modulation of spin states in single-atom catalysts but also sets a new precedent for advancing sustainable ammonia synthesis, a critical challenge in the realm of green chemistry. Overall, our computational results deliver compelling evidence of the pivotal role of spin state modulation via interfacial engineering, demonstrating a useful way to discover future innovations in materials science and catalysis.

■ ASSOCIATED CONTENT

ⓢ Supporting Information

The Supporting Information is available free of charge at https://pubs.acs.org/doi/10.1021/jacsau.4c00030.

Free energy calculations, SISSO model, geometry structures, relative stability, AIMD simulation, band structures, PDOS of Fe, charge density and spin density distribution, supercell size and solvation effect, comparison with other works, scaling relations between electronic properties of TM atom, Fe, and their connecting atoms, d-band center, primary features, training and test results by SISSO model, other spin and activity descriptor, changes in charge and spin moments of Fe with TM concentration, ΔG (*N$_2$), ΔG (*N$_2$ → *N$_2$H), and ΔG (*NH$_2$ → *NH$_3$) as a function of TM atoms, free energy changes of all elementary steps through three pathways, free energy corrections, the related results for other functional and other systems, self-conservation (PDF)

■ AUTHOR INFORMATION

Corresponding Authors

Shaobin Tang − *Key Laboratory of Organo-Pharmaceutical Chemistry of Jiangxi Province, Gannan Normal University, Ganzhou 341000, China;* ⓞ orcid.org/0000-0002-2969-8698; Email: tsb1980@xmu.edu.cn

Jun Jiang − *Key Laboratory of Precision and Intelligent Chemistry, School of Chemistry and Materials Science, University of Science and Technology of China, Hefei, Anhui 230026, China;* ⓞ orcid.org/0000-0002-6116-5605; Email: jiangj1@ustc.edu.cn

Xin Xu − *Collaborative Innovation Center of Chemistry for Energy Materials, Shanghai Key Laboratory of Molecular Catalysis and Innovative Materials, MOE Key Laboratory of Computational Physical Sciences, Department of Chemistry, Fudan University, Shanghai 200438, China;* ⓞ orcid.org/0000-0002-5247-2937; Email: xxchem@fudan.edu.cn

Authors

Yuqin Zhang − *Key Laboratory of Organo-Pharmaceutical Chemistry of Jiangxi Province, Gannan Normal University, Ganzhou 341000, China*

Da Wang − *School of Mathematics and Computer Science, Gannan Normal University, Ganzhou 341000, China*

Guanping Wei − *Key Laboratory of Organo-Pharmaceutical Chemistry of Jiangxi Province, Gannan Normal University, Ganzhou 341000, China*

Baolei Li − *School of Mathematics and Computer Science, Gannan Normal University, Ganzhou 341000, China*

Zongchang Mao − *Key Laboratory of Organo-Pharmaceutical Chemistry of Jiangxi Province, Gannan Normal University, Ganzhou 341000, China*

Si-Min Xu − *Key Laboratory of Organo-Pharmaceutical Chemistry of Jiangxi Province, Gannan Normal University, Ganzhou 341000, China*

Zhenyu Li − *Key Laboratory of Precision and Intelligent Chemistry, School of Chemistry and Materials Science, University of Science and Technology of China, Hefei, Anhui 230026, China;* ⓞ orcid.org/0000-0003-2112-9834

Xijun Wang − *Department of Chemical and Biological Engineering, Northwestern University, Evanston, Illinois 60208, United States;* ⓞ orcid.org/0000-0001-9155-7653

Complete contact information is available at:
https://pubs.acs.org/10.1021/jacsau.4c00030

Author Contributions

S.T. and J.J. conceived the idea and supervised the project. Y.Z., G.W., Z.M., S.X., X.W., and Z.L. carried out the theoretical calculations, which involved DFT and AIMD simulations. D.W., B.L., X.W., and J.J. utilized the machine learning model to predict the spin moments. Y.Z., S.T., X.W., and X.X. cowrote the paper. All authors discussed the results and commented on the manuscript.

Notes

The authors declare no competing financial interest.

■ REFERENCES

(1) Zhao, J.-X.; Chen, Z.-F. Single Mo Atom Supported on Defective Boron Nitride Monolayer as an Efficient Electrocatalyst for Nitrogen Fixation: A Computational Study. *J. Am. Chem. Soc.* **2017**, *139*, 12480−12487.

(2) Han, L.-L.; Liu, X.-J.; Chen, J.-P.; Lin, R.-Q.; Liu, H.-X.; Lü, F.; Bak, S.; Liang, Z.-X.; Zhao, S.-Z.; Stavitski, E.; Luo, J.; Adzic, R. R.; Xin, H.-L. Atomically Dispersed Molybdenum Catalysts for Efficient Ambient Nitrogen Fixation. *Angew. Chem., Int. Ed.* **2019**, *58*, 2321−2325.

(3) Zhuo, H.-Y.; Zhang, X.; Liang, J.-X.; Yu, Q.; Xiao, H.; Li, J. Theoretical Understandings of Graphene-based Metal Single-Atom Catalysts: Stability and Catalytic Performance. *Chem. Rev.* **2020**, *120*, 12315−12341.

(4) Liu, X.; Jiao, Y.; Zheng, Y.; Jaroniec, M.; Qiao, S.-Z. Building Up a Picture of the Electrocatalytic Nitrogen Reduction Activity of Transition Metal Single-Atom Catalysts. *J. Am. Chem. Soc.* **2019**, *141*, 9664−9672.

(5) Légaré, M.-A.; Bélanger-Chabot, G.; Dewhurst, R. D.; Welz, E.; Krummenacher, I.; Engels, B.; Braunschweig, H. Nitrogen Fixation and Reduction at Boron. *Science* **2018**, *359*, 896−900.

(6) Li, X.-F.; Li, Q.-K.; Cheng, J.; Liu, L.-L.; Yan, Q.; Wu, Y.-C.; Zhang, X.-H.; Wang, Z.-Y.; Qiu, Q.; Luo, Y. Conversion of Dinitrogen to Ammonia by FeN$_3$-Embedded Graphene. *J. Am. Chem. Soc.* **2016**, *138*, 8706−8709.

(7) Li, J.; Sougrati, M. T.; Zitolo, A.; Ablett, J. M.; Oğuz, I. C.; Mineva, T.; Matanovic, I.; Atanassov, P.; Huang, Y.; Zenyuk, I.; Di Cicco, A.; Kumar, K.; Dubau, L.; Maillard, F.; Dražić, G.; Jaouen, F. Identification of Durable and Non-durable FeN$_x$ Sites in Fe-N-C Materials for Proton Exchange Membrane Fuel Cells. *Nat. Catal.* **2021**, *4*, 10−19.

(8) Li, X.-N.; Cao, C.-S.; Hung, S.-F.; Lu, Y.-R.; Cai, W.-Z.; Rykov, A. I.; Miao, S.; Xi, S.-B.; Yang, H.-B.; Hu, Z.-H.; Wang, J.-H.; Zhao, J.-Y.; Alp, E. E.; Xu, W.; Chan, T.-S.; Chen, H.-M.; Xiong, Q.-H.; Xiao, H.; Huang, Y.-Q.; Li, J.; Zhang, T.; Liu, B. Identification of the Electronic and Structural Dynamics of Catalytic Centers in Single-Fe-atom Material. *Chem.* 2020, 6, 3440−3454.

(9) Zhong, W.-H.; Qiu, Y.; Shen, H.-J.; Wang, X.-J.; Yuan, J.-Y.; Jia, C.-Y.; Bi, S.-W.; Jiang, J. Electronic Spin Moment As a Catalytic Descriptor for Fe Single-Atom Catalysts Supported on C_2N. *J. Am. Chem. Soc.* 2021, 143, 4405−4413.

(10) Garcés-Pineda, F. A.; Blasco-Ahicart, M.; Nieto-Castro, D.; López, N.; Galán-Mascarós, J. R. Direct Magnetic Enhancement of Electrocatalytic Water Oxidation in Alkaline Media. *Nat. Energy* 2019, 4, 519−525.

(11) Gong, Y.-N.; Zhong, W.-H.; Li, Y.; Qiu, Y.-Z.; Zheng, L.-R.; Jiang, J.; Jiang, H.-L. Regulating Photocatalysis by Spin-State Manipulation of Cobalt in Covalent Organic Frameworks. *J. Am. Chem. Soc.* 2020, 142, 16723−16731.

(12) Liu, J.-C.; Ma, X.-L.; Li, Y.; Wang, Y.-G.; Xiao, H.; Li, J. Heterogeneous Fe_3 Single-Cluster Catalyst for Ammonia Synthesis via an Associative Mechanism. *Nat. Commun.* 2018, 9, 1610.

(13) Sun, Z.-M.; Lin, L.; He, J.-L.; Ding, D.-J.; Wang, T.-Y.; Li, J.; Li, M.-X.; Liu, Y.-C.; Li, Y.-Y.; Yuan, M.-W.; Huang, B.-B.; Li, H.-F.; Sun, G.-B. Regulating the Spin State of Fe^{III} Enhances the Magnetic Effect of the Molecular Catalysis Mechanism. *J. Am. Chem. Soc.* 2022, 144, 8204−8213.

(14) Qu, K.; Zheng, Y.; Jiao, Y.; Zhang, X.; Dai, S.; Qiao, S. Polydopamine-Inspired, Dual Heteroatom-Doped Carbon Nanotubes for Highly Efficient Overall Water Splitting. *Adv. Energy Mater.* 2017, 7, 1602068.

(15) Liu, K.; Fu, J.; Lin, Y.; Luo, T.; Ni, G.; Li, H.; Lin, Z.; Liu, M. Insights into the Activity of Single-Atom Fe-N-C Catalysts for Oxygen Reduction Reaction. *Nat. Commun.* 2022, 13, 2075.

(16) Liu, W.-G.; Zhang, L.-L.; Liu, X.; Liu, X.-Y.; Yang, X.-F.; Miao, S.; Wang, W.-T.; Wang, A.-Q.; Zhang, T. Discriminating Catalytically Active FeN_x Species of Atomically Dispersed Fe-N-C Catalyst for Selective Oxidation of the C-H Bond. *J. Am. Chem. Soc.* 2017, 139, 10790−10798.

(17) Tang, C.; Zhang, Q. Nanocarbon for Oxygen Reduction Electrocatalysis: Dopants, Edges, and Defects. *Adv. Mater.* 2017, 29, 1604103.

(18) Xie, E.; Wang, X.-J. Fine-Tuning Dual Single-Atom Metal Sites on Graphene toward Enhanced Oxygen Reduction Reaction Activity. *J. Phys. Chem. Lett.* 2023, 14, 9392−9402.

(19) He, T.; Chen, Y.; Liu, Q.; Lu, B.; Song, X.; Liu, H.; Liu, M.; Liu, Y.-N.; Zhang, Y.; Ouyang, X.; Chen, S. Theory-Guided Regulation of FeN_4 Spin State by Neighboring Cu Atoms for Enhanced Oxygen Reduction Electrocatalysis in Flexible Metal-Air Batteries. *Angew. Chem., Int. Ed.* 2022, 61, e202201007.

(20) Lin, C.-C.; Liu, T.-R.; Lin, S.-R.; Boopathi, K. M.; Chiang, C.-H.; Tzeng, W.-Y.; Chien, W. H. C.; Hsu, H.-S.; Luo, C.-W.; Tsai, H.-Y.; Chen, H.-A.; Kuo, P.-C.; Shiue, J.; Chiou, J.-W.; Pong, W.-F.; Chen, C.-C.; Chen, C.-W. Spin-Polarized Photocatalytic CO_2 Reduction of Mn-Doped Perovskite Nanoplates. *J. Am. Chem. Soc.* 2022, 144, 15718−15726.

(21) Garcés-Pineda, F. A.; Blasco-Ahicart, M.; Nieto-Castro, D.; López, N.; Galán-Mascarós, J. R. Direct Magnetic Enhancement of Electrocatalytic Water Oxidation in Alkaline Media. *Nat. Energy* 2019, 4, 519−525.

(22) Dang, Q.; Tang, S.-B.; Liu, T.-Y.; Li, X.-K.; Wang, X.-J.; Zhong, W.-H.; Luo, Y.; Jiang, J. Regulating Electronic Spin Moments of Single-Atom Catalyst Sites via Single-Atom Promoter Tuning on S-Vacancy MoS_2 for Efficient Nitrogen Fixation. *J. Phys. Chem. Lett.* 2021, 12, 8355−8362.

(23) Zhao, X.-X.; Song, P.; Wang, C.-C.; Riis-Jensen, A. C.; Fu, W.; Deng, Y.; Wan, D.-Y.; Kang, L.-X.; Ning, S.-C.; Dan, J.-D.; Venkatesan, T.; Liu, Z.; Zhou, W.; Thygesen, K. S.; Luo, X.; Pennycook, S. J.; Loh, K. P. Engineering Covalently Bonded 2D Layered Materials by Self-Intercalation. *Nature* 2020, 581, 171−177.

(24) Gong, Y.; Yuan, H.; Wu, C. L.; Tang, P.; Yang, S. Z.; Yang, A.; Li, G.; Liu, B.; van de Groep, J.; Brongersma, M. L.; Chisholm, M. F.; Zhang, S. C.; Zhou, W.; Cui, Y. Spatially Controlled Doping of Two-Dimensional SnS_2 through Intercalation for Electronics. *Nat. Nanotechnol.* 2018, 13, 294−299.

(25) Kim, S.; Maassen, J.; Lee, J.; Kim, S. M.; Han, G.; Kwon, J.; Hong, S.; Park, J.; Liu, N.; Park, Y. C.; Omkaram, I.; Rhyee, J.; Hong, Y. K.; Yoon, Y. Interstitial Mo-Assisted Photovoltaic Effect in Multilayer $MoSe_2$ Phototransistors. *Adv. Mater.* 2018, 30, 1705542.

(26) Wan, J.-Y.; Lacey, S. D.; Dai, J.-Q.; Bao, W.-Z.; Fuhrer, M. S.; Hu, L.-B. Tuning Two-Dimensional Nanomaterials by Intercalation: Materials, Properties and Applications. *Chem. Soc. Rev.* 2016, 45, 6742−6765.

(27) Wordsworth, J.; Benedetti, T. M.; Somerville, S. V.; Schuhmann, W.; Tilley, R. D.; Gooding, J. J. The Influence of Nanoconfinement on Electrocatalysis. *Angew. Chem., Int. Ed.* 2022, 61, e202200755.

(28) O'Mara, P. B.; Wilde, P.; Benedetti, T. M.; Andronescu, C.; Cheong, S.; Gooding, J. J.; Tilley, R. D.; Schuhmann, W. Cascade Reactions in Nanozymes: Spatially Separated Active Sites inside Ag-Core-Porous-Cu-Shell Nanoparticles for Multistep Carbon Dioxide Reduction to Higher Organic Molecules. *J. Am. Chem. Soc.* 2019, 141, 14093−14097.

(29) Jiang, Z.; Zhou, W.; Hu, C.; Luo, X.; Zeng, W.; Gong, X.; Yang, Y.; Yu, T.; Lei, W.; Yuan, C. Interlayer-Confined NiFe Dual Atoms within MoS_2 Electrocatalyst for Ultra-Efficient Acidic Overall Water Splitting. *Adv. Mater.* 2023, 35, 2300505.

(30) Deng, J.; Deng, D.; Bao, X. Robust Catalysis on 2D Materials Encapsulating Metals: Concept, Application, and Perspective. *Adv. Mater.* 2017, 29, 1606967.

(31) Chen, J. G.; Crooks, R. M.; Seefeldt, L. C.; Bren, K. L.; Bullock, R. M.; Darensbourg, M. Y.; Holland, P. L.; Hoffman, B.; Janik, M. J.; Jones, A. K.; Kanatzidis, M. G.; King, P.; Lancaster, K. M.; Lymar, S. V.; Pfromm, P.; Schneider, W. F.; Schrock, R. R. Beyond Fossil Fueldriven Nitrogen Transformations. *Science* 2018, 360, eaar6611.

(32) Hao, Y.-C.; Guo, Y.; Chen, L.-W.; Shu, M.; Wang, X.-Y.; Bu, T.-A.; Gao, W.-Y.; Zhang, N.; Su, X.; Feng, X.; Zhou, J.-W.; Wang, B.; Hu, C.-W.; Yin, A.-X.; Si, R.; Zhang, Y.-W.; Yan, C.-H. Promoting Nitrogen Electroreduction to Ammonia with Bismuth Nanocrystals and Potassium Cations in Water. *Nat. Catal.* 2019, 2, 448−456.

(33) Zhang, L.; Ji, X.; Ren, X.; Ma, Y.; Shi, X.; Tian, Z.; Asiri, A. M.; Chen, L.; Tang, B.; Sun, X. Electrochemical Ammonia Synthesis via Nitrogen Reduction Reaction on a MoS_2 Catalyst: Theoretical and Experimental Studies. *Adv. Mater.* 2018, 30, 1800191.

(34) Li, S.-J.; Bao, D.; Shi, M.-M.; Wulan, B. R.; Yan, J.-M.; Jiang, Q. Amorphizing of Au Nanoparticles by CeO_x-RGO Hybrid Support towards Highly Efficient Electrocatalyst for N_2 Reduction under Ambient Conditions. *Adv. Mater.* 2017, 29, 1700001.

(35) Jin, H.; Li, L.; Liu, X.; Tang, C.; Xu, W.; Chen, S.; Song, L.; Zheng, Y.; Qiao, S.-Z. Nitrogen Vacancies on 2D Layered W_2N_3: A Stable and Efficient Active Site for Nitrogen Reduction Reaction. *Adv. Mater.* 2019, 31, 1902709.

(36) Zhang, L.-L.; Ding, L.-X.; Chen, G.-F.; Yang, X.-F.; Wang, H.-H. Ammonia Synthesis under Ambient Conditions: Selective Electroreduction of Dinitrogen to Ammonia on Black Phosphorus Nanosheets. *Angew. Chem., Int. Ed.* 2019, 58, 2612−2616.

(37) Azofra, L. M.; Li, N.; MacFarlane, D. R.; Sun, C.-H. Promising Prospects for 2D d^2-d^4 M_3C_2 Transition Metal Carbides (MXenes) in N_2 Capture and Conversion into Ammonia. *Energy Environ. Sci.* 2016, 9, 2545−2549.

(38) Creutz, S. E.; Peters, J. C. Catalytic Reduction of N_2 to NH_3 by an Fe-N_2 Complex Featuring a C-Atom Anchor. *J. Am. Chem. Soc.* 2014, 136, 1105−1115.

(39) Rodriguez, M. M.; Bill, E.; Brennessel, W. W.; Holland, P. L. N_2 Reduction and Hydrogenation to Ammonia by a Molecular Iron-Potassium Complex. *Science* 2011, 334, 780−783.

(40) He, T.; Chen, Y.; Liu, Q.; Lu, B.; Song, X.; Liu, H.; Liu, M.; Liu, Y.-N.; Zhang, Y.; Ouyang, X.; Chen, S. Theory-Guided Regulation of FeN_4 Spin State by Neighboring Cu Atoms for

Enhanced Oxygen Reduction Electrocatalysis in Flexible Metal-Air Batteries. *Angew. Chem., Int. Ed.* **2022**, *61*, e202201007.

(41) Dai, Y.; Liu, B.; Zhang, Z.; Guo, P.; Liu, C.; Zhang, Y.; Zhao, L.; Wang, Z. Tailoring the d-Orbital Splitting Manner of Single Atomic Sites for Enhanced Oxygen Reduction. *Adv. Mater.* **2023**, *35*, 2210757.

(42) Liu, W.-G.; Zhang, L.-L.; Liu, X.; Liu, X.-Y.; Yang, X.-F.; Miao, S.; Wang, W.-T.; Wang, A.-Q.; Zhang, T. Discriminating Catalytically Active FeN$_x$ Species of Atomically Dispersed Fe-N-C Catalyst for Selective Oxidation of the C-H Bond. *J. Am. Chem. Soc.* **2017**, *139*, 10790−10798.

(43) Li, X.-F.; Li, Q.-K.; Cheng, J.; Liu, L.-L.; Yan, Q.; Wu, Y.-C.; Zhang, X.-H.; Wang, Z.-Y.; Qiu, Q.; Luo, Y. Conversion of Dinitrogen to Ammonia by FeN$_3$-Embedded Graphene. *J. Am. Chem. Soc.* **2016**, *138*, 8706−8709.

(44) Jin, Z.-Y.; Li, P.-P.; Meng, Y.; Fang, Z.-W.; Xiao, D.; Yu, G.-H. Understanding the Inter-Site Distance Effect in Single-Atom Catalysts for Oxygen Electroreduction. *Nat. Catal.* **2021**, *4*, 615−522.

(45) Guo, X.-Y.; Huang, S.-P. Tuning Nitrogen Reduction Reaction Activity via Controllable Fe Magnetic Moment: A Computational study of Single Fe Atom Supported on Defective Graphene. *Electrochim. Acta* **2018**, *284*, 392−399.

(46) Perdew, J. P.; Wang, Y. Accurate and Simple Analytic Representation of the Electron-Gas Correlation Energy. *Phys. Rev. B* **1992**, *45*, 13244−13249.

(47) Kresse, G.; Hafner, J. Ab Initio Molecular Dynamics for Liquid Metals. *Phys. Rev. B* **1993**, *47*, 558−561.

(48) Perdew, J. P.; Burke, K.; Ernzerhof, M. Generalized Gradient Approximation Made Simple. *Phys. Rev. Lett.* **1996**, *77*, 3865−3868.

(49) Grimme, S.; Antony, J.; Ehrlich, S.; Krieg, H. A Consistent and Accurate Ab Initio Parametrization of Density Functional Dispersion Correction (DFT-D) for the 94 Elements H-Pu. *J. Chem. Phys.* **2010**, *132*, 154104.

(50) Henkelman, G.; Arnaldsson, A.; Jónsson, H. A Fast and Robust Algorithm for Bader Decomposition of Charge Density. *Comput. Mater. Sci.* **2006**, *36*, 354−360.

(51) Sanville, E.; Kenny, S. D.; Smith, R.; Henkelman, G. Improved Grid-Based Algorithm for Bader Charge Allocation. *J. Comput. Chem.* **2007**, *28*, 899−908.

(52) Manz, T. A.; Limas, N. G. Introducing DDEC6 Atomic Population Analysis: Part 1. Charge Partitioning Theory and Methodology. *RSC Adv.* **2016**, *6*, 47771−47801.

(53) Limas, N. G.; Manz, T. A. Introducing DDEC6 Atomic Population Analysis: Part 4. Efficient Parallel Computation of Net Atomic Charges, Atomic Spin Moments, Bond Orders, and More. *RSC Adv.* **2018**, *8*, 2678−2707.

(54) Mortazavi, M.; Wang, C.; Deng, J.-K.; Shenoy, V. B.; Medhekar, N. V. Ab Initio Characterization of Layered MoS$_2$ as Anode for Sodium-Ion Batteries. *J. Power Sources* **2014**, *268*, 279−286.

(55) Heyd, J.; Scuseria, G. E.; Ernzerhof, M. Hybrid Functionals Based on a Screened Coulomb Potential. *J. Chem. Phys.* **2003**, *118*, 8207−8215.

(56) Heyd, J.; Scuseria, G. E.; Ernzerhof, M. Erratum: "Hybrid Functionals Based on a Screened Coulomb Potential. *J. Chem. Phys.* **2006**, *124*, 219906.

(57) Anisimov, V. I.; Aryasetiawan, F.; Lichtenstein, A. I. First-Principles Calculations of the Electronic Structure and Spectra of Strongly Correlated Systems: the LDA+U Method. *J. Phys.: Condens. Matter* **1997**, *9*, 767.

(58) Ali, M. E.; Sanyal, B.; Oppeneer, P. M. Electronic Structure, Spin-States, and Spin-Crossover Reaction of Heme-Related Fe-Porphyrins: A Theoretical Perspective. *J. Phys. Chem. B* **2012**, *116*, 5849−5859.

(59) Mathew, K.; Sundararaman, R.; Letchworth-Weaver, K.; Arias, T. A.; Hennig, R. G. Implicit Solvation Model for Density-Functional Study of Nanocrystal Surfaces and Reaction Pathways. *J. Chem. Phys.* **2014**, *140*, No. 084106.

(60) Ouyang, R.-H.; Curtarolo, S.; Ahmetcik, E.; Scheffler, M.; Ghiringhelli, L. M. SISSO: A Compressed-Sensing Method for Identifying the Best Low-Dimensional Descriptor in an Immensity of Offered Candidates. *Phys. Rev. Mater.* **2018**, *2*, No. 083802.

(61) Chang, X.; Zhao, Z.-J.; Lu, Z.-P.; Chen, S.; Luo, R.; Zha, S.-J.; Li, L.-L.; Sun, G.-D.; Pei, C.-L.; Gong, J.-L. Designing Single-Site Alloy Catalysts Using a Degree-of-isolation Descriptor. *Nat. Nanotechnol.* **2023**, *18*, 611−616.

(62) Jiang, C.; Song, H.; Sun, G.; Chang, X.; Zhen, S.; Wu, S.; Zhao, Z.-J.; Gong, J. Data-Driven Interpretable Descriptors for the Structure-Activity Relationship of Surface Lattice Oxygen on Doped Vanadium Oxides. *Angew. Chem., Int. Ed.* **2022**, *61*, e202206758.

(63) Ren, C.-J.; Lu, S.-H.; Wu, Y.-L.; Ouyang, Y.-X.; Zhang, Y.-H.; Li, Q.; Ling, C.-Y.; Wang, J.-L. A Universal Descriptor for Complicated Interfacial Effects on Electrochemical Reduction Reactions. *J. Am. Chem. Soc.* **2022**, *144*, 12874−12883.

(64) Fang, C.; An, W. Single-Metal-Atom site with High-Spin State Embedded in Defective BN Nanosheet Promotes Electrocatalytic Nitrogen Reduction. *Nano Res.* **2021**, *14*, 4211−4219.

(65) Choi, C.; Back, S.; Kim, N.-Y.; Lim, J.; Kim, Y.-H.; Jung, Y. Suppression of Hydrogen Evolution Reaction in Electrochemical N$_2$ Reduction Using Single-Atom Catalysts: A Computational Guideline. *ACS Catal.* **2018**, *8*, 7517−7525.

(66) Zhang, H.-C.; Cui, C.-N.; Luo, Z.-Y. MoS$_2$-Supported Fe$_2$ Clusters Catalyzing Nitrogen Reduction Reaction to Produce Ammonia. *J. Phys. Chem. C* **2020**, *124*, 6260−6266.

(67) Xie, K.; Wang, F.-T.; Wei, F.-F.; Zhao, J.; Lin, S. Revealing the Origin of Nitrogen Electroreduction Activity of Molybdenum Disulfide Supported Iron Atoms. *J. Phys. Chem. C* **2022**, *126*, 5180−5188.

(68) Guo, R.-X.; An, W.; Liu, M.-M.; Li, Y.-Y.; Wang, Y.-B.; Yang, S.-B.; Men, Y.; Wang, J.-G.; Liu, S. Modulating the Coordination Environment of Active Site Structure for Enhanced Electrochemical Nitrogen Reduction: The Mechanistic Insight and an Effective Descriptor. *Appl. Surf. Sci.* **2024**, *644*, No. 158799.

(69) Wang, Y.-Y.; Ren, X.-Y.; Jiang, B.-J.; Deng, M.; Zhao, X.-J.; Pang, R.; Li, S. F. Synergetic Catalysis of Magnetic Single-Atom Catalysts Confined in Graphitic-C$_3$N$_4$/CeO$_2$(111) Heterojunction for CO Oxidization. *J. Phys. Chem. Lett.* **2022**, *13*, 6367−6375.

(70) Zhang, L.-Y.; Ren, X.-Y.; Zhao, X.-J.; Zhu, Y.-D.; Pang, R.; Cui, P.; Jia, Y.; Li, S.-F.; Zhang, Z.-Y. Synergetic Charge Transfer and Spin Selection in CO Oxidation at Neighboring Magnetic Single-Atom Catalyst Sites. *Nano Lett.* **2022**, *22*, 3744−3750.